# EventPS: Real-Time Photometric Stereo Using an Event Camera Supplementary Material

Bohan Yu[1,2] Jieji Ren[3] Jin Han[4,5] Feishi Wang[1,2] Jinxiu Liang[1,2] Boxin Shi[1,2*]

[1] National Key Laboratory for Multimedia Information Processing, School of Computer Science, Peking University

[2] National Engineering Research Center of Visual Technology, School of Computer Science, Peking University

[3] School of Mechanical Engineering, Shanghai Jiao Tong University

[4] Graduate School of Information Science and Technology, The University of Tokyo [5] National Institute of Informatics

{ybh1998, wangfeishi, cssherryliang, shiboxin}@pku.edu.cn

jiejiren@sjtu.edu.cn, jinhan@nii.ac.jp

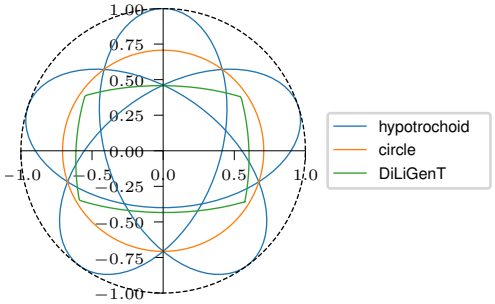


Figure 12. Three types of scanning patterns used in our experiments. All the "circle", "hypotrochoid", and "DiLiGenT" patterns are used on the synthetic dataset for training.

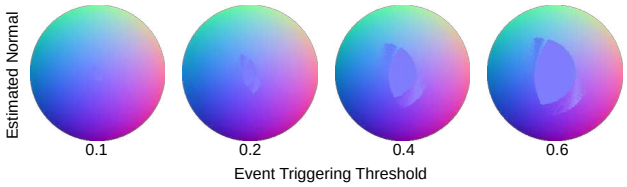


Figure 13. Normal estimation results with blind area (at the center of each sphere). As the event triggering threshold increases, the size of the blind area will also become larger.

## 6. Scanning Pattern and Blind Area

According to Sec. 4.1, we implement 3 scanning patterns for illumination. These scanning patterns are shown in Fig. 12. We chose the "circle" scanning pattern in our real validation platform for its mechanical feasibility. However, a blind area issue exists in this pattern.

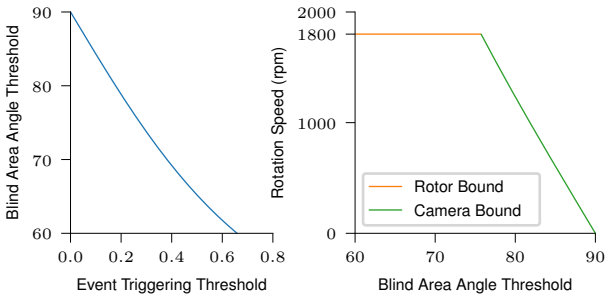


Figure 14. Blind area simulation results for a sphere object. Left: Blind area angle threshold w.r.t. event triggering threshold. Right: Rotation speed w.r.t. blind area angle threshold. Under limited event triggering rate, reducing the rotation speed allows us to set a lower event triggering threshold, achieving a higher blind area angle threshold (smaller blind area size) and better normal estimation sensitivity.

**Blind area.** According to Fig. 4, using the "circle" scanning pattern, the radiance change becomes smaller as the elevation angle of the surface normal increases. When the radiance change is smaller than the triggering threshold of the event camera, no event is triggered. In this situation, we can only infer that the elevation angle is above a specific threshold. However, we cannot determine the exact normal direction. We call the part of the surface under this situation the blind area. As shown in Fig. 13, there is a blind area at the center of each sphere, where the normal elevation angle is above a threshold $\theta_t$. The size of the blind area is related to the event triggering threshold. The elevation angle threshold $\theta_t$ of the blind area is the solution of the following equation:

$$\cos\left(\theta_t - \theta_{\mathbf{L}}\right) = \exp(2C)\cos(\pi - \theta_t - \theta_{\mathbf{L}}), \qquad (12)$$

*Corresponding author: Boxin Shi

where $\theta_{\mathbf{L}}$ is the elevation angle of the light source, and $C$ is the event triggering threshold. The brightest reflection ($\cos(\theta_t - \theta_{\mathbf{L}})$) and the dimmest reflection ($\cos(\pi - \theta_t - \theta_{\mathbf{L}})$) differ by $2C$, where 2 positive events (and 2 negative events) are triggered, which is the minimal requirement to satisfy the condition to solve Eq. (10). When the elevation angle of the surface point $\theta$ is greater than the threshold $\theta_t$, fewer than 2 null space vectors are generated, resulting in the blind area with unsolvable surface normal. We show an example simulation result in Fig. 14. From the left figure, we can see that the blind area elevation angle threshold decreases as we decrease the event triggering threshold. The more advanced "hypotrochoid" does not suffer from the blind area issue. Thanks to the varying lighting elevation angle design, events are triggered even with a flat plane. However, it is more difficult to implement on the real validation platform.

**PS quality w.r.t. rotation speed.** According to Sec. 4.2, we limit the light source rotation speed to 240 rpm in real dataset capturing for better quality. To reduce the blind area size, we need to decrease the event-triggering threshold. As a result, more events are triggered, reaching the event rate upper bound of the camera (100 M events per second). There are two limitations on rotation speed: rotor bound (It is unsafe to push this rotor beyond 1800 rpm. Otherwise, the high-speed moving parts may cause injury to the experiment operator if they rupture.), and camera bound (This camera generates at most 100 M events per second). In Fig. 14, we show a simulation result with sphere in the right figure. The rotation speed requires to be decreased for higher blind area elevation angle threshold (smaller bind area size) to prevent event dropping. We limit the rotation speed in compensation for a better normal estimation sensitivity. The theoretical blind area elevation angle threshold is about 87° at 240 rpm.

## 7. FramePS trilemma

In the photometric stereo experimental setup, the data rate of a frame-based camera is the joint effect of three terms: the number of exposure bracketing images, the number of light directions per round, and the light scanning speed. However, the frame-based camera can never achieve optimal configuration of these three terms at the same time due to its limited bandwidth. As shown in Fig. 15, we analyze the trilemma of frame-based camera in details: (TL1) Capturing a significant number of exposure bracketing images along with various light directions per round is time-consuming. Consequently, object movement during this period results in motion blur in the recovered normal map. (TL2) To balance a good number of light directions per round and scanning speed, we have to disable exposure bracketing. With the limited dynamic range, the result would be affected by surface albedo. (TL3) To achieve efficient scanning speed and exposure bracketing, the number of light directions per round must be reduced. As a result, the quality of the estimated normal maps degrades for the lack of information. When a frame-based camera tries to optimize two of these factors, it has to compromise on the third one, which affects the quality of the estimated normal maps.

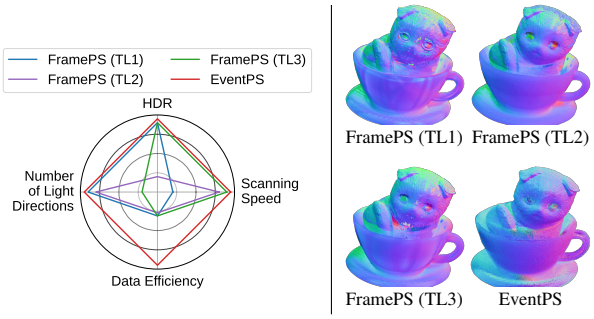


Figure 15. Left: Performance comparison between FramePS under three configurations (TL1 - TL3) and EventPS. Right: Estimated normal maps for all cases. The results demonstrate the trilemma of FramePS: (TL1) scanning speed, (TL2) HDR, and (TL3) number of light directions cannot be fulfilled simultaneously. In contrast, the proposed EventPS satisfies all three criteria with the best bandwidth efficiency.

In our EventPS, the HDR advantage and compression capability of an event camera allow us to fulfill all three criteria while maintaining bandwidth efficiency. Therefore, compared to FramePS, EventPS shows more advantages in practical scenarios.

## 8. Dynamic Scene Validation

**Validation platform.** In Fig. 16, we present a detailed depiction of the equipment utilized for dynamic scene validation. We transfer the rotation of the DC motor to a synchronized hollow drum rotor using a timing belt. In this way, we can place the event camera view point in the middle of the scanning pattern to observe the object through the central hole. Most of the frames and parts are 3D printed and the corresponding 3D mesh files will be released upon the acceptance of this paper.

**Dynamic scene video.** The video is available as a separate file named "EventPS_supp_video.mp4". During the dynamic scene real-time demo, we set the parameters of the event camera as follows: The "bandwidth bias (bias_fo)" is set to $-35$, the two "contrast sensitivity threshold biases" are both set to $-10$, and the "dead time bias" is set to $-20$.

## 9. Complete Evaluation Results

We show all the objects used in our experiments in Fig. 17 and the complete estimated normal map and error map in

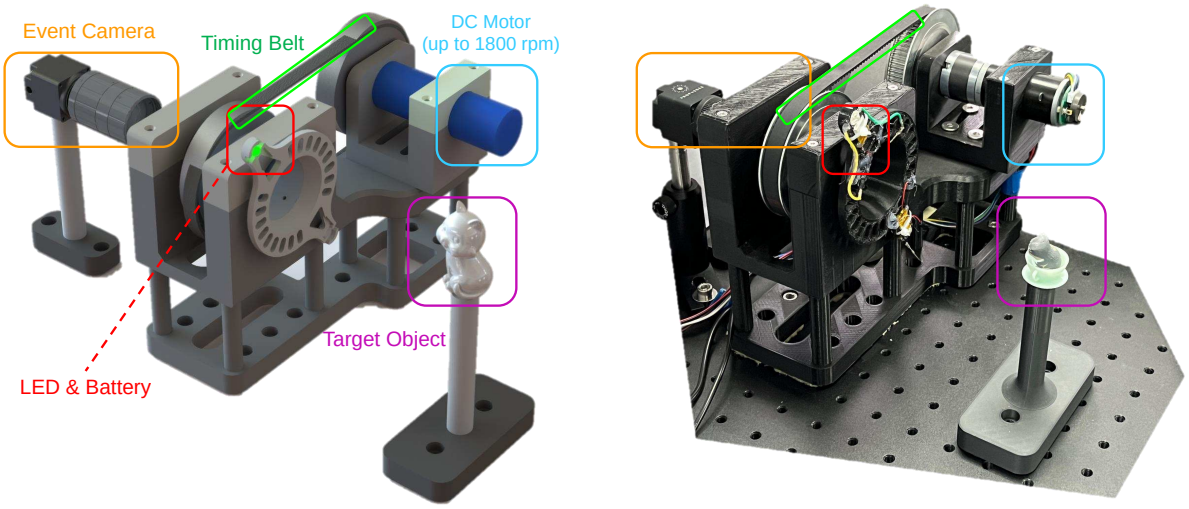


Figure 16. Components of the proposed validation platform. The rendered image (left) aligns with the viewpoint of the photographed real platform (right) and is consistent with the supplementary video.


Figure 17. All the objects used in our experiments. Upper: Static objects in the real dataset for quantitative experiments. Lower: Rotating or deformable objects used for dynamic scene qualitative experiments.

Fig. 18 (on DiLiGenT-Ev semi-real dataset) and Fig. 19 (on the real dataset).

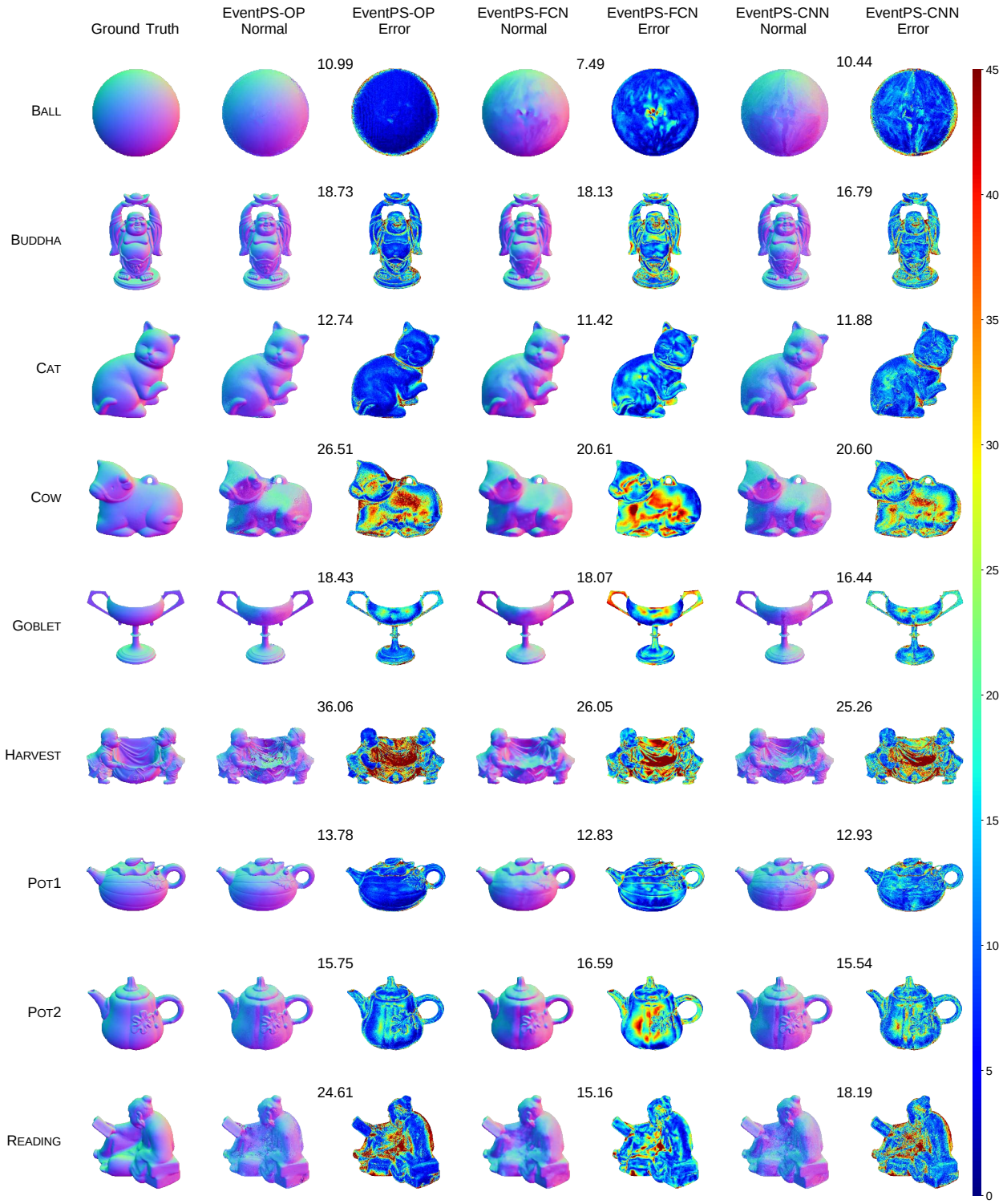


Figure 18. Complete evaluation results on the DiLiGenT-Ev semi-real dataset. The results demonstrate consistent and stable performance among all objects of our EventPS algorithms.

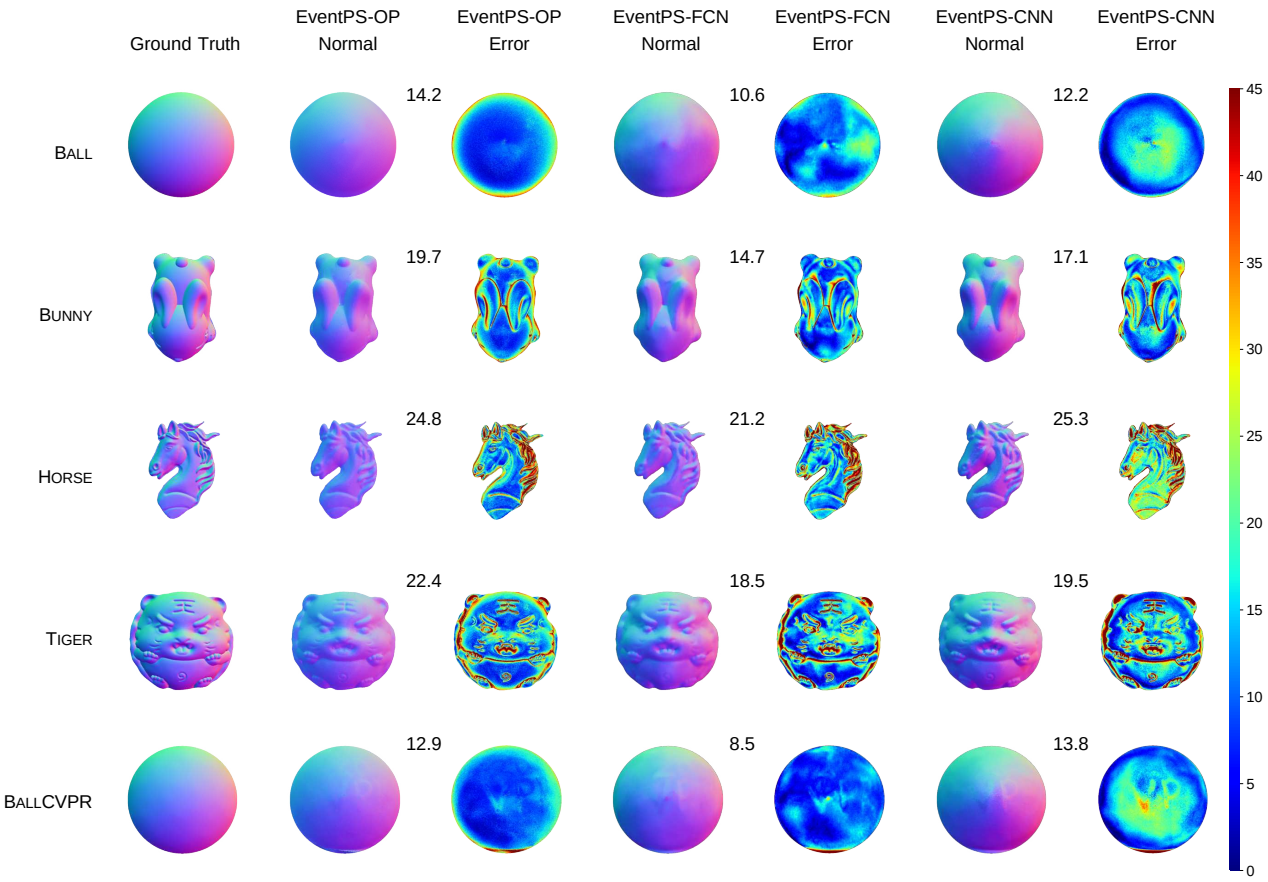


Figure 19. Complete evaluation results on the real dataset. The results demonstrate consistent and stable performance among all objects of our EventPS algorithms.